Supplementary Section

S1. Theory for FDPM-based Tomographic Reconstruction

This section briefly describes the changes made to the CW-based algorithm for NIRF tomography (Lu *et al* 2011), derived using the third-order simplified spherical harmonics (SP_3) approximation to the radiative transfer equation (RTE), to allow time-dependent measurements using frequency-domain approach. As compared to the CW-based algorithm, the measured fluence at excitation and emission wavelengths is complex in nature, given by $\phi^{[x,m]} = I_{AC}^{[x,m]} e^{-j\theta[x,m]}$, where $[x,m]$ denotes the variables at excitation ($[x]$) or emission ($[m]$) wavelengths, respectively. The tissue absorption coefficient can be expressed as $\mu_a^{[x,m]} + i\omega / c_{x,m}$, where $\mu_a^{[x,m]}$ is the absorption coefficient of the tissue at the excitation/emission wavelengths in CW mode; ω is the modulation frequency; and $c_{x,m}$ is the speed of light at excitation/emission wavelengths within the tissues.

Using the SP_3 approximation along with relevant boundary conditions (Klose *et al* 2006, Chu *et al* 2009, Lu *et al* 2010), and after a series of deductions, we get

$$\left[J^{+,m,b}\right] = [G]\left[\mu_a^{[f]}\right], \tag{1}$$

where G indicates the relationship matrix between $J^{+,m,b}$ and fluorescent absorption distribution $\mu_a^{[f]}$; superscript b represents the variables present only at the tissue surface; $J^{+,m,b}$ is the measurable exiting partial current for the emission wavelength and given by

$$\begin{aligned} J^{+,m,b} &= J_R^{+,m,b} + iJ_i^{+,m,b} \\ &= \left(\frac{1}{4} + J_0\right)\left(\varphi_1^{[m]} - \frac{2}{3}\varphi_2^{[m]}\right) - \left(\frac{0.5 + J_1}{3\mu_{a1}^{[m]}}\right) v.\nabla\,\varphi_1^{[m]} \\ &+ \frac{1}{3}\left(\frac{5}{16} + J_2\right)\varphi_2^{[m]} - \left(\frac{J_3}{7\mu_{a3}^{[m]}}\right) v.\nabla\,\varphi_2^{[m]} \end{aligned}, \tag{2}$$

where the coefficients $J_0,\ldots,J_3$ are found in (Klose *et al* 2006), $J_R^{+,m,b}$ and $J_I^{+,m,b}$ are the real and imaginary parts of $J^{+,m,b}$; v is the outgoing unit vector normal to the boundary; $\varphi_{1,2}^{[x,m]}$ are complex variables and denotes the *composite moments* of the *Legendre moments* for excitation and emission radiances; $\mu_{a,i}^{[m]}$ denotes the i-th (i = 1,2,3) absorption coefficients at emission wavelengths and is equal to $\mu_a^{[m]} + \mu_s^{[m]}(1-g^i) + i\omega / c_{x,m}$; $\mu_s^{[m]}$ is the tissue scattering coefficient at the emission wavelength; and g is the anisotropic factor. Rewriting (1) after including complex characteristics we get

$$\begin{bmatrix} J_R^{+,m,b} \\ J_I^{+,m,b} \end{bmatrix} = \begin{bmatrix} G_R \\ G_I \end{bmatrix}\left[\mu_a^{[f]}\right], \tag{3}$$

where G_R and G_I are the real and imaginary parts of G. When there are multiple illuminations (N_v) at different positions, we get

$$J_T^{+,m,b} = A\mu_a^{[f]}, \tag{4}$$

where

$$J_T^{+,m,b} = \begin{bmatrix} J_R^{+,m,b,1} \\ J_I^{+,m,b,1} \\ J_R^{+,m,b,2} \\ J_I^{+,m,b,2} \\ \dots \\ J_R^{+,m,b,N_v} \\ J_I^{+,m,b,N_v} \end{bmatrix} \quad A = \begin{bmatrix} G_R^1 \\ G_I^1 \\ G_R^2 \\ G_I^2 \\ \dots \\ G_R^{N_v} \\ G_I^{N_v} \end{bmatrix}. \tag{5}$$

We have used limited memory variable metric-bound constrained quasi-Newton method (BLMVM) (Benson *et al* 2001) to solve the following least squares problem for fluorescence recovery:

$$\min \theta(\mu_a^{[f]}) : \left\| A\mu_a^{[f]} - J_T^{+,m,b} \right\|^2 \text{ subject to } 0 < \mu_a^{[f]} < \mu_a^{f,\sup}, \tag{6}$$

where $\mu_a^{f,\sup}$ is the upper constraint on $\mu_a^{[f]}$.

S2. Assessment of Measurement Precision

Since accuracy of tomographic reconstructions depends critically on precision of the input data, it is necessary to benchmark the precision of the FDPM system by evaluating and reducing the errors associated with measurements of I_{AC} and θ. To assess the errors, a white paper was placed between the laser diode and detector, and illuminated by a diffused 5 cm^2 homogeneous distribution of excitation light (100 $\mu W/cm^2$). A neutral density filter with optical density of 5 was placed in front of the camera lens to protect the intensifier from oversaturation as well as to maximize the dynamic range of the CCD. The CCD array was binned down from 1024 x 1024 pixels to 128 x 128 pixels in order to improve the SNR. The intensity of the scattered excitation light was measured to assess the precision of the I_{AC} and θ measurements. In order to evaluate improved measurement precision as a function of the instrument settings, the CCD integration times were varied between 400 ms, 600 ms, and 800 ms, N was changed between 16, 32, 64, and 128, and the experiment was repeated over M times between 5, 10, 20, to 40. The total data acquisition time was the product of M, N, and CCD integration time for each frame, and excludes time required for readout and charge digitization. The STD of I_{AC} and θ values was then evaluated as function of M, N, and integration times. The I_{AC} error was calculated by taking the ratio of its STD recorded over M cycles to its mean while the θ error was defined as the STD in the measured phase. The I_{AC} and θ precision were computed on a pixel-by-pixel basis and were then averaged over the entire homogeneously illuminated area. The results are shown in Table S1.

Table S1. Measurement precision represented by I_{AC} and θ errors.

CCD integration time (ms)	Number of phase-delays (N)	Number of repeated cycles (M)	Amplitude (I_{AC}) error (±%)	Phase (θ) error (±°)	Mean I_{DC} (excitation counts (e.c.))
800	128	5	0.70	0.33	36802
	64	10	0.84	0.49	36864
	32	20	1.21	0.69	37025
	16	40	1.67	0.98	37827
600	128	5	0.70	0.38	28073
	64	10	0.97	0.56	28053
	32	20	1.37	0.81	28154
	16	40	1.95	1.15	28276
400	128	5	0.82	0.47	18509
	64	10	1.20	0.69	18877
	32	20	1.65	0.97	19224
	16	40	2.37	1.38	19565

Furthermore, Figure S1 shows that upon capturing more photons through increased CCD integration times or upon use of higher intensifier gain the I_{AC} (Figure S1(a)) and θ (Figure S1(b)) errors reduce considerably implying the positive influence of higher SNR on measurement precision.

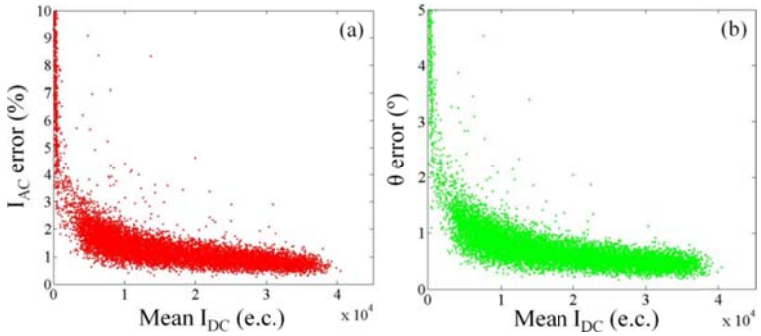

Figure S1. Effect of increased photon counts on measurement precision. (a) I_{AC} error (defined as the ratio of STD in I_{AC} recorded over M cycles to its mean I_{DC}), and (b) θ error (defined as STD in phase over M cycles) plotted as a function of I_{DC} over the entire image intensifier area.

Figure S2(a) shows the I_{DC} SNR plotted as a function of I_{DC} in order to analyze the noise sources affecting the measurements. SNR for any given pixel was determined by calculating the ratio of I_{DC} to STD of I_{DC} measured over M number of images per phase-delay, where I_{DC} is the average intensity of the pixel. It can be observed that the plot (Figure S2(a)) shows a linear dependence between the I_{DC} SNR and mean I_{DC}. For better visualization, the mean I_{DC} data points were grouped together into smaller bins, as seen in Figure S2(b), with each bin having a length of 200 counts along the x-axis. All the data points in that bin were then averaged. Thus, any given data point along the x-axis in Figure S2(b) represents an average of the mean I_{DC} data points collected in that bin for which max(mean I_{DC}) – min(mean I_{DC}) ≤ 200 counts. The y-axis represents the average of the I_{DC} SNR data points corresponding to the mean I_{DC} data points collected in that bin. In addition, for comparison, a graph with '+' data-markers plots square root of the binned mean I_{DC} data as a function of the binned mean I_{DC}. This plot runs parallel to the I_{DC} SNR for mean I_{DC} >5000 counts and implies that the I_{DC} SNR displays square-root dependence that is typical of photon-noise-limited operation for the ICCD detectors (Frenkel *et al* 1997). The result therefore indicates that photon-noise is the major noise source limiting the detection ability of ICCD detectors.

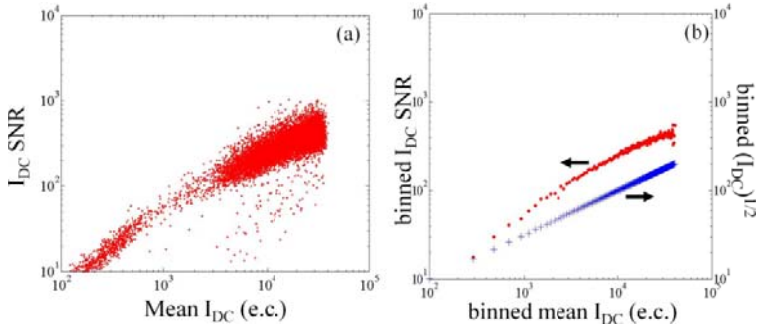

Figure S2. Photon-noise limited operation for ICCD detectors. (a) Relationship between the I_{DC} SNR and mean I_{DC} data. The data was gathered over the entire image intensifier area using 800 ms CCD integration time measured with N = 64. For better comprehension the data from (a) was collected in bins, averaged, and plotted in (b) as represented by marker '●' (red color). The plot with '+' (blue color) marker indicates the square-root of the binned mean I_{DC} data.

S3. Tomographic Imaging in Phantoms with Varying Thresholds

Figure S3 highlights the effect of thresholding on the reconstructed figure quality. As a specific example, we have chosen reconstruction results obtained from measurements performed in gantry setting with 4-projections, as shown in Figure 7. Figure S3 shows phantom reconstructions by imposing variable thresholding (top 80-100% of the maximum reconstructed value). It can be observed that in the absence of thresholding (100%) additional reconstructed volumes can be seen on the phantom surface as well as few around the actual target within the tissue. The values on these reconstructed artifacts are very small. However, their presence makes it difficult to appreciate

the improvement in reconstruction quality upon increasing the number of projections, as shown in Figure 7. It also demonstrates that by choosing a suitable thresholding value the surface artifacts that are away from the tissue of interest can be removed from the reconstructed image and hence do not contribute meaningfully to the tomography.

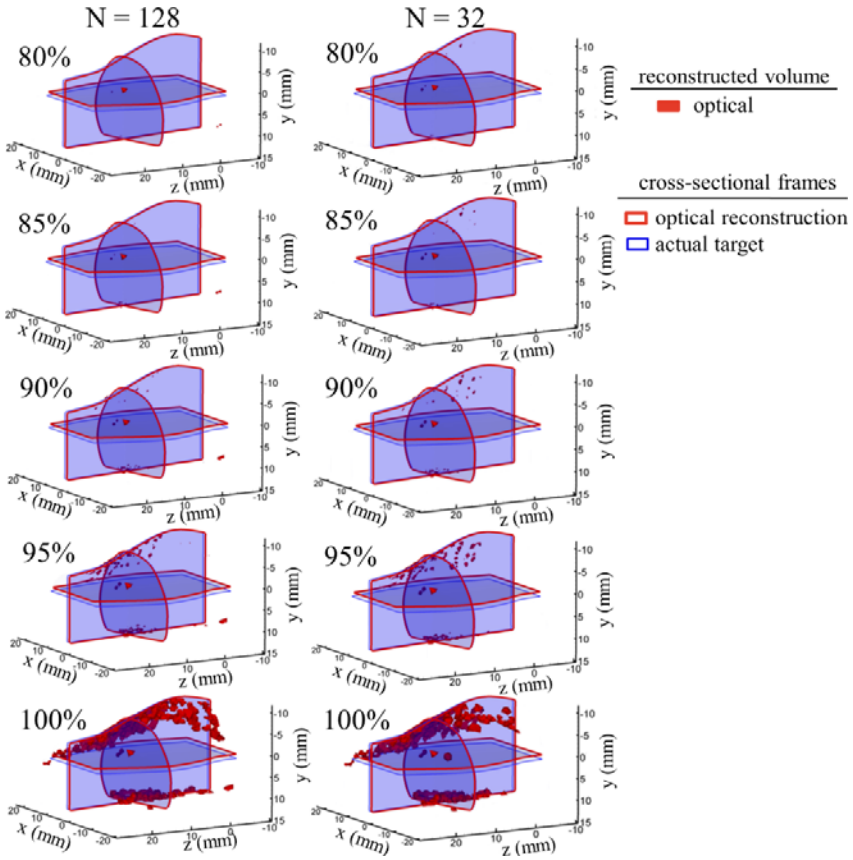

Figure S3. Phantom reconstructions imposed with variable thresholding are shown for measurements performed using gantry setting, 4-projections, and different phase-delays (*N*), as shown in Figures 7 (i, k). A threshold of 80% indicates that the top 80% of the maximum reconstructed value has been retained.

References

Benson S J and Mo´re J 2001 A limited-memory variable-metric algorithm for bound-constrained minimization *Technical Report* ANL/MCS-P909-0901, Mathematics and Computer Science Division, Argonne National Laboratory, Argonne, IL

Chu M, Vishwanath K, Klose A D and Dehghani H 2009 Light transport in biological tissue using three-dimensional frequency-domain simplified spherical harmonics equations *Phys. Med. Biol.* **54** 2493-509

Frenkel A, Sartor M A and Wlodawski M S 1997 Photon-noise-limited operation of intensified CCD cameras *Appl. Optics* **36** 5288-97

Klose A D and Larsen E W 2006 Light transport in biological tissue based on the simplified spherical harmonics equations *J. Comput. Phys.* **220** 441-70

Lu Y, Zhu B, Darne C, Tan I-Chih, Rasmussen J C and Sevick-Muraca E M 2011 Improvement of fluorescence-enhanced optical tomography with improved optical filtering and accurate model-based reconstruction algorithms *J. Biomed. Opt.* **16** 126002-1-4

Lu Y, Zhu B, Shen H, Rasmussen J C, Wang G and Sevick-Muraca E M 2010 A parallel adaptive finite element simplified spherical harmonics approximation solver for frequency domain fluorescence molecular imaging *Phys. Med. Biol.* **55** 4625-45